

# Geophysical Research Letters<sup>®</sup>



## RESEARCH LETTER

10.1029/2023GL103716

### Key Points:

- The effect of droplet collision-coalescence on the aerosol size distribution is analyzed in three-dimensional simulations
- Collision-coalescence processing introduces a characteristic bimodality in the aerosol size distribution
- The large-scale stratocumulus dynamics are key to the development of a stable population of processed aerosol particles

### Supporting Information:

Supporting Information may be found in the online version of this article.

### Correspondence to:

F. Hoffmann,  
fa.hoffmann@lmu.de

### Citation:

Hoffmann, F., & Feingold, G. (2023). A note on aerosol processing by droplet collision-coalescence. *Geophysical Research Letters*, 50, e2023GL103716. <https://doi.org/10.1029/2023GL103716>

Received 15 MAR 2023

Accepted 21 MAY 2023

### Author Contributions:

**Conceptualization:** Fabian Hoffmann, Graham Feingold

**Data curation:** Fabian Hoffmann

**Formal analysis:** Fabian Hoffmann, Graham Feingold

**Funding acquisition:** Fabian Hoffmann

**Investigation:** Fabian Hoffmann

**Methodology:** Fabian Hoffmann, Graham Feingold

**Project Administration:** Fabian Hoffmann

**Software:** Fabian Hoffmann



**Validation:** Fabian Hoffmann

**Visualization:** Fabian Hoffmann

© 2023. The Authors. Geophysical Research Letters published by Wiley Periodicals LLC on behalf of American Geophysical Union.

This is an open access article under the terms of the [Creative Commons Attribution License](https://creativecommons.org/licenses/by/4.0/), which permits use, distribution and reproduction in any medium, provided the original work is properly cited.

## A Note on Aerosol Processing by Droplet Collision-Coalescence

Fabian Hoffmann<sup>1</sup>  and Graham Feingold<sup>2</sup> 

<sup>1</sup>Meteorologisches Institut, Ludwig-Maximilians-Universität München, Munich, Germany, <sup>2</sup>Chemical Sciences Laboratory, NOAA/Earth System Research Laboratories, Boulder, CO, USA

**Abstract** The processing of aerosol by droplet collision-coalescence is analyzed in three-dimensional simulations of drizzling stratocumulus using a Lagrangian cloud model for the representation of aerosol and cloud microphysics. Collision-coalescence processing is shown to create a characteristic bimodality in the aerosol size distribution. We show that the large-scale dynamics of the stratocumulus-topped boundary layer are key to understanding the amount of time available for collision-coalescence processing. The large-scale dynamics enable aerosol particles to repeat a cycle of droplet condensation, collision-coalescence, and evaporation, which causes a steady increase in aerosol size. This process is continued until the aerosol grows so large that droplet growth is substantially accelerated and multiple collisions occur within one cycle, forming precipitation-sized droplets that are lost to the surface, including the aerosol. An analytical relationship is derived that captures the fundamental shape of the processed aerosol size distribution.

**Plain Language Summary** Clouds consist of cloud droplets, and cloud droplets grow from aerosol particles, which are tiny particles suspended in the atmosphere. But clouds also modify aerosol particles. This study shows that the merging of cloud droplets, a process related to the production of rain, can lead to larger aerosol particles, causing characteristic changes in the aerosol size distribution that are revealed in this study. These changes are important because larger aerosol particles will create cloud droplets more easily, with commensurate effects on the development of clouds.

## 1. Introduction

Aerosol particles affect clouds and hence the climate. Most fundamentally, aerosol particles serve as cloud condensation nuclei and thus control the number and size of cloud droplets, determining cloud radiative properties (e.g., Albrecht, 1989; Twomey, 1977), the development of precipitation (e.g., Squires, 1958), and even the turbulent mixing of clouds with their environment (e.g., Bretherton et al., 2007; Wang et al., 2003). But aerosol particles do not only affect clouds, they are also affected by clouds (e.g., Hudson et al., 2018). Clouds are the ideal environment for aqueous chemistry to add aerosol mass, for example, by the oxidation of sulfur dioxide (e.g., Hegg & Hobbs, 1979; Hoppel et al., 1986; Jaruga & Pawlowska, 2018). Furthermore, cloud droplets can collect unactivated aerosol particles by Brownian capture (e.g., Svenningsson et al., 1997). The subject of this study will, however, be the collision and subsequent coalescence of cloud droplets, merging the dissolved aerosol masses inside them to form larger particles upon evaporation (e.g., Flossmann et al., 1985; Hudson & Noble, 2020, 2022; Noble & Hudson, 2019). As these processes shape the aerosol size distribution, they alter the ability of aerosol particles to activate to cloud droplets and to act as drizzle embryos, and thus feed back on the aforementioned effects of aerosol particles on clouds and the climate.

Fundamentally, the aerosol size distribution is defined as

$$n_a = \frac{dN_a}{dr_a}, \quad (1)$$

describing the number of aerosol particles exhibiting sizes in an infinitesimal aerosol radius range between  $r_a$  and  $r_a + dr_a$ , where  $N_a$  is the cumulative aerosol concentration. Thus, representing changes in  $n_a$  by cloud processing requires a two-dimensional modeling framework that predicts changes in  $r_a$ , as well as the concurrent cloud microphysical changes in the droplet liquid radius  $r_d$ . Accordingly, more sophisticated modeling approaches than those applied for studying cloud microphysics alone are needed. For instance, Flossmann et al. (1985) and Lebo and Seinfeld (2011) developed two-dimensional aerosol-cloud microphysical models that predict the simultaneous development of the discretized (or binned)  $r_a$  and  $r_d$  distributions. By coupling a bin aerosol model to a bin

Writing – original draft: Fabian Hoffmann  
Writing – review & editing: Graham Feingold

microphysical model and calculating the transfer of aerosol solute mass between drops based on the transfer of the water mass, Feingold et al. (1996) and more recently Zeng and Li (2023) provided a more computationally efficient alternative. However, this approach is only able to calculate general (moment-based) changes in the processed aerosol size distribution. The treatment of aerosol and cloud processes in bulk aerosol-cloud microphysical models is too simple to resolve more than the average change in aerosol particle size (e.g., Berner et al., 2013).

Over the last decade, these so-called Eulerian approaches have been complemented by Lagrangian cloud models (LCMs) that represent cloud microphysical processes by individually simulated computational particles, which allow for the detailed tracking of  $r_a$  and  $r_d$  in the simulated hydrometeors (e.g., Arabas et al., 2015; Chandrakar et al., 2022; Hoffmann et al., 2015; Shima et al., 2009). Thus, LCMs provide a highly detailed alternative to understand changes in the aerosol and cloud droplet size distribution, subject to some limitations (e.g., Hill et al., 2023). In this study, we apply an LCM coupled to a high-resolution large-eddy simulation (LES) model to understand the processing of aerosol by collision and coalescence.

This note is organized as follows. First, we will briefly introduce the LCM-LES framework and its setup, before simulation results are presented (Section 2). Based on these results, we will develop a theory to understand the changes in the aerosol size distribution (Section 3). The main results of this note are summarized in Section 4.

## 2. Simulations

### 2.1. Setup

All simulations have been carried out using the LES *System for Atmospheric Modeling* (SAM) (Khairoutdinov & Randall, 2003), fully coupled to the LCM by Hoffmann et al. (2015). Here, we summarize the most relevant parts of this modeling framework, with details furnished in the references below. The LCM represents hydrometeors, that are, aerosol particles, cloud droplets, and rain drops, as computational particles. Due to computational restrictions, not all hydrometeors are simulated explicitly, and every computational particle represents a multitude of identical hydrometeors, while microphysical processes and interactions are scaled accordingly. It is assumed that aerosol particles never fully dry, that is, always accumulate some water. The activation of aerosol particles to cloud droplets and their further growth by condensation by solving the diffusional growth equation, including Köhler theory (Hoffmann et al., 2015; Köhler, 1936). Gravitational collision and coalescence is represented using a statistical approach (Hoffmann et al., 2017), with collision efficiencies by Hall (1980). A coalescence efficiency of unity is assumed. Brownian capture (e.g., Svenningsson et al., 1997) is neglected. All particles are moved by the mean LES wind, fall by sedimentation using terminal velocities by Beard (1976), and experience stochastic velocity fluctuations to represent LES-unresolved turbulent motions (Weil et al., 2004). Note that the LCM does not categorize hydrometeors into aerosol, cloud droplets, or rain to apply the aforementioned microphysical processes. The relevance of a process to a specific hydrometeor is determined by the underlying physics.

For this study, a weakly drizzling nocturnal maritime stratocumulus is simulated. The case is based on the second research flight of the DYCOMS-II campaign (Stevens et al., 2003), assuming fixed surface fluxes, subsidence, and a simple parameterization for longwave radiative cooling, with further details given in Ackerman et al. (2009). The model domain is  $7.2 \times 7.2 \times 2.88 \text{ km}^3$  in the horizontal and vertical directions, with respective grid spacings of  $50 \times 50 \times 5 \text{ m}^3$ .

Three simulations with different initial aerosol distributions are investigated. These aerosol distributions are created by assigning an  $r_a$  to each computational particle. These  $r_a$  are obtained from a random generator that follows a lognormal distribution, which is typical for aerosol (e.g., Jaenicke, 1993). The geometric standard deviation of the lognormal distribution is 1.25 for all cases, but the geometric mean radius  $r_{a,m}$  is varied from 12.5 nm to 25 nm to 50 nm, creating a typical Aitken mode. Here, we mainly discuss results from the 25 nm case, with further analysis provided in Supporting Information S1. For all three cases the initial aerosol concentration is  $40 \text{ cm}^{-3}$ . The initial number of computational particles per LES grid box is 50, which is sufficient for the successful representation of the aforementioned microphysical processes (Unterstrasser et al., 2020). The number of hydrometeors represented by each computational particle is the same for all particles initially, but changes due to collision and coalescence during the course of the simulation. Computational particles are initialized up to a height of 1,000 m, that is, well above the maximum height of the stratocumulus-topped boundary layer, which varies between 800 and 830 m in the conducted simulations. During initialization, all particles are initialized as

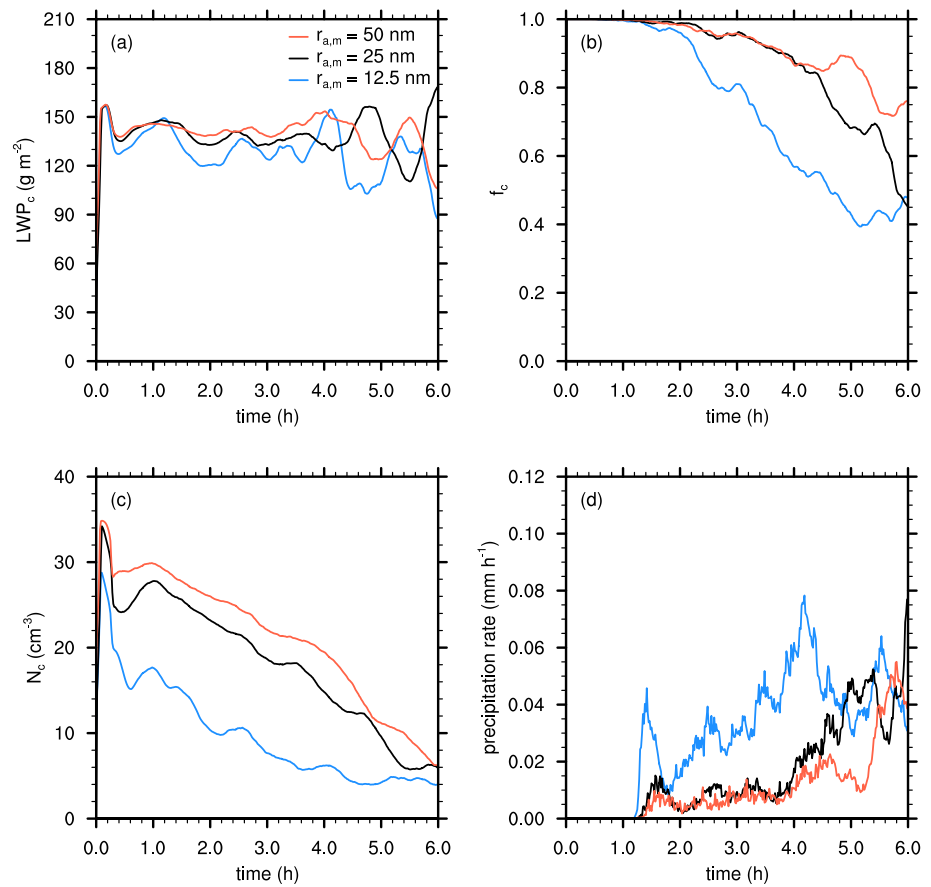


**Figure 1.** Time series of (a) the in-cloud LWP<sub>c</sub>, (b) *f*<sub>c</sub>, (c) *N*<sub>c</sub>, and (d) the surface precipitation rate for *r*<sub>a,m</sub> = 12.5 nm (blue lines), 25 nm (black lines), and 50 nm (red lines).

haze, and their liquid water radius is equilibrated to the relative humidity of their surroundings. Within the cloud layer, the particles are equilibrated to a relative humidity of 0.99 at the first timestep. Afterward, the particles are allowed to grow by condensation, but collision-coalescence and sedimentation remain disabled for the first hour of the simulation.

The simulation is run for 6 hr, with a timestep of 0.5 s. This timestep is applied for the LES and the LCM, but subcycled for condensational growth if necessary. Previous studies have shown that a timestep of 0.5 s is sufficient for representing collision-coalescence in the LCM (e.g., Unterstrasser et al., 2020).

## 2.2. Results

The general development of the simulations is presented in Figure 1, showing (a) the vertically integrated, in-cloud liquid water path LWP<sub>c</sub>, (b) cloud fraction *f*<sub>c</sub>, (c) in-cloud droplet concentration *N*<sub>c</sub>, and (d) the surface precipitation rate for the three analyzed aerosol size distributions. On average, the LWP<sub>c</sub> remains relatively constant at about 140 g m<sup>-2</sup> for all simulated cases, but fluctuates increasingly as the simulation progresses. These fluctuations reflect the breaking up of the cloud deck after the onset of precipitation, which is visible in the steady decrease in *f*<sub>c</sub> from full cloud cover at 1 hr of simulated time toward values between 0.75 and 0.5 at the end of the simulation at 6 hr, depending on the prescribed aerosol size distribution. Changes in *N*<sub>c</sub> during the first hour of simulated time are an artifact of the developing turbulence in the simulated boundary layer (model spin-up), and should therefore be discarded. Afterward, *N*<sub>c</sub> decreases steadily from about 30 to less than 10 cm<sup>-3</sup> as collision-coalescence merges cloud droplets to rain drops. The lowest values of *f*<sub>c</sub> and *N*<sub>c</sub> occur for the smallest aerosol particles, that is, *r*<sub>a,m</sub> = 12.5 nm (blue line), for which activation to cloud droplets is least likely. The commensurately lower *N*<sub>c</sub> favors subsequent droplet growth by condensation and hence collision-coalescence.

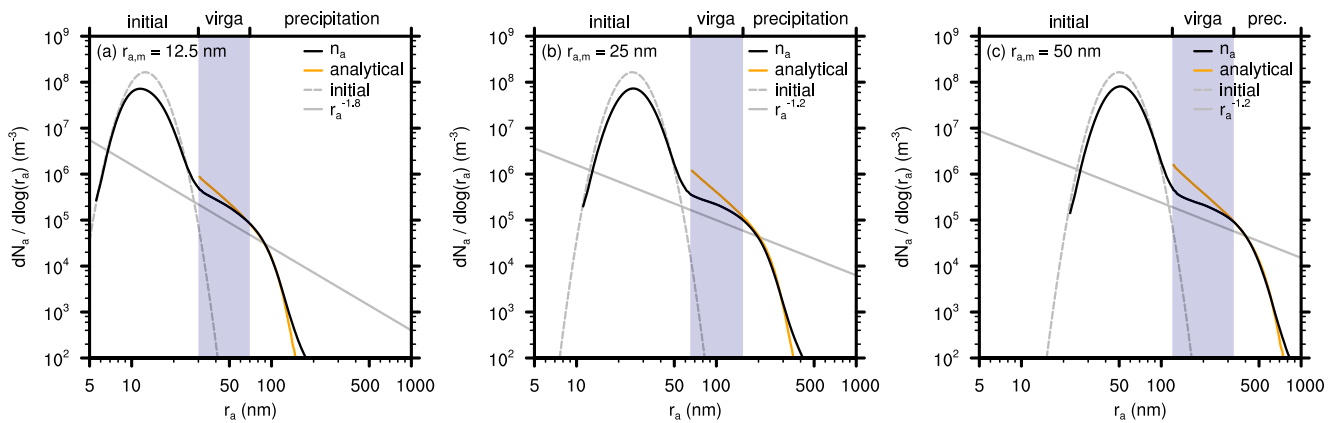


**Figure 2.** The processed aerosol size distribution  $n_a^c = dN_a / d\log(r_a)$  (black lines) for (a)  $r_{a,m} = 12.5$  nm, (b)  $r_{a,m} = 25$  nm, and (c)  $r_{a,m} = 50$  nm. Results are overlaid with their respective initial aerosol size distributions (dashed gray lines). Section 3 discusses the analytical solution (orange lines), as well as the slopes that approximate the virga range (continuous gray lines) in more detail. The upper abscissa denotes the initial, virga, and precipitation ranges of the aerosol size spectrum; the virga range is highlighted in pale blue.

Nonetheless, the precipitation rate is rather weak for all simulated cases. Overall, all simulated cases are similar to the results presented in Ackerman et al. (2009).

The effects of these dynamical and microphysical processes on the aerosol size distribution are shown in Figure 2, depicting  $n_a^c = dN_a / d\log(r_a) = \ln(10) r_a n_a$  for all simulated aerosol size distributions. Note that  $n_a^c$  is determined from all (activated and deactivated) aerosol particles in the lowermost 1,000 m of the simulation domain, capturing the entire stratocumulus-topped boundary layer, as well as a small fraction of the free-troposphere. Furthermore,  $n_a^c$  is averaged over the last hour of the simulation.

All simulated aerosol size distributions (black lines in Figure 2) show one mode, which is relatively close to its respective initial aerosol size distribution (dashed gray lines), and a newly developed mode with a constant slope between  $-1.8$  and  $-1.2$  toward larger  $r_a$  (continuous gray lines) that falls off sharply for even larger  $r_a$ . As we will show in more detail below, this new mode is caused by the collision-coalescence processing of aerosol that shifts aerosol particles from the initial distribution to larger  $r_a$ , thereby naturally decreasing the number of aerosol particles. Note, however, that for  $r_{a,m} = 12.5$  nm, the aerosol size distribution agrees well with the initial aerosol size distribution for  $r_a < 10$  nm, reflecting that these particles are too small to activate and thus do not participate in collision-coalescence processing. For the following analysis, we will split the aerosol size distributions into three distinct regions, which we will call the initial, virga, and precipitation ranges, based on the predominant microphysical processes. These ranges are denoted on the upper abscissae of Figures 2 and 3 (and Figures S1 and S2 in Supporting Information S1), where the virga range is highlighted in pale blue, with the initial and precipitation ranges found toward smaller and larger  $r_a$ , respectively. Further note that these ranges are not as distinct as indicated, and transition zones exist between them.

For the  $r_{a,m} = 25$  nm aerosol size distribution, Figure 3 shows (a) the droplet radius  $\bar{r}_d$ , (b) aerosol growth rate  $\bar{c}_a = \overline{dr_a/dt}$ , (c) time between two collisions experienced by a collector droplet  $\overline{\Delta t_{coll}}$ , and (d) relative tendencies  $\overline{d\ln(n_a)/dt}$  for the activation of droplets (blue line), deactivation (black line), net collision gain rate (orange line), and precipitation loss rate (red line) as a function of  $r_a$ . The overbar indicates that these are  $r_a$ -bin-averaged quantities, that is, they are obtained as the average of all values that fall within a specific  $r_a$ -bin. In particular,  $\bar{r}_d$  is determined from the total liquid water mass per  $r_a$  bin, including the water from cloud droplets and unactivated aerosol particles (haze). As before, the data are averaged over the last hour of the simulation, and the lower-most 1,000 m of the model domain. Results for the simulations with  $r_{a,m} = 12.5$  and 50 nm are similar, and thus only shown in Supporting Information S1.

$\bar{r}_d$  is smallest in the initial range (Figure 3a). The reason for this is that the cloud layer represents only a small fraction of the analyzed boundary layer ( $\sim 30\%$ ), and hence only a commensurately small fraction of aerosol particles activate to cloud droplets (blue line Figure 3d). Thus, the average  $\bar{r}_d$  is rather small. However, the asymmetry between the activation and deactivation rates in the initial range indicates that some of these particles are inside the cloud and hence large enough to participate in collision-coalescence (blue and black lines in Figure 3d), causing the deactivation of collected particles at larger size than their prior size. At larger  $r_a$ , more particles tend to exist inside the cloud only, which is indicated by the substantially larger  $\bar{r}_d$  toward the virga range. The increase in  $\bar{c}_a$  (Figure 3b), which is only possible due to collision-coalescence of cloud droplets, indicates that these

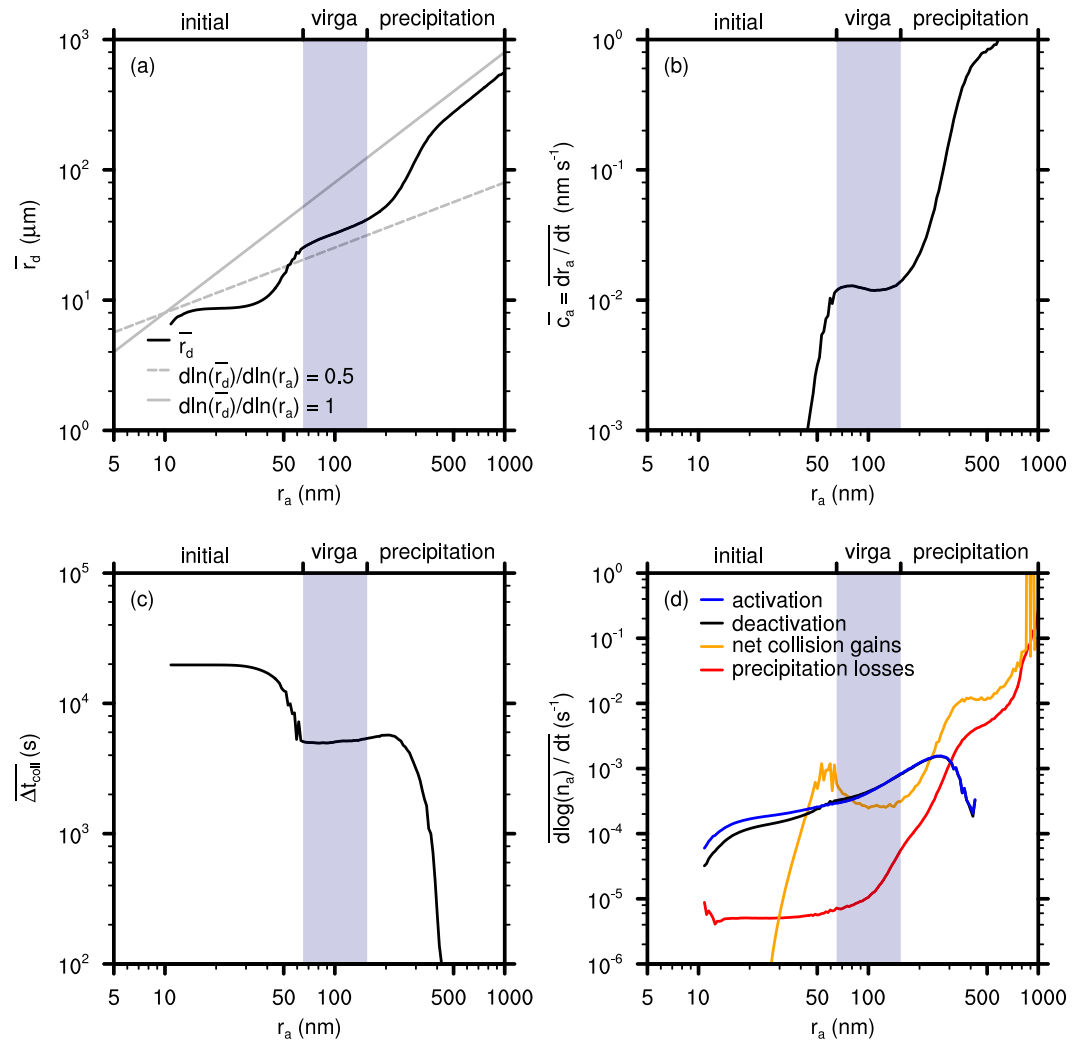


**Figure 3.** The distribution of the  $r_a$ -bin-averaged (a) droplet radius  $\bar{r}_d$ , (b)  $\bar{c}_a = \overline{dr_a/dt}$ , (c) time between two collisions experienced by a collector droplet  $\overline{\Delta t_{\text{coll}}}$ , and (d) relative tendencies  $d\ln(n_a)/dt$  for the activation of droplets (blue line), deactivation (black line), net collision gain rate (orange line), and precipitation loss rate (red line) as a function of  $r_a$ . The results are shown for  $r_{a,m} = 25$  nm. The upper abscissa denotes the initial, virga, and precipitation ranges of the aerosol size spectrum; the virga range is highlighted in pale blue.

particles are a product of droplet collision-coalescence, which is confirmed by the concurrent decrease in  $\overline{\Delta t_{\text{coll}}}$  (Figure 3c) and the increase in the net collision gain rate (orange line in Figure 3d).

While  $\bar{r}_d$  and  $\bar{c}_a$  increase with  $r_a$  in the precipitation range (Figures 3a and 3b), the virga range exhibits only slight differences in these quantities, as discussed in more detail in the following paragraphs. In the precipitation range, however, droplets collide frequently, as reflected in the sharp decrease in  $\overline{\Delta t_{\text{coll}}}$  (Figure 3c) and the strong increase in the net collision gain rate (orange line in Figure 3d). At the same time, precipitation losses (red line in Figure 3d) increase, and begin to match the net collision gain rate for  $r_a > 800$  nm. Moreover, there are no activation and deactivation events for  $r_a > 500$  nm (blue and black lines in Figure 3d), which indicates that all particles that exist in this part of the precipitation range have entered it as a cloud or rain drop and are lost to the surface without sufficient evaporation to cause deactivation. Thus, no permanent population of these particles is created, which is also visible in the strong decrease in  $n_a^e$  presented in Figure 2.

The most interesting part of the aerosol spectrum is the virga range, which eschews the rather simple interpretations of the initial and precipitation range that are dominated by either the initial aerosol distribution or the loss of aerosol by precipitation to the surface, respectively. Key to understanding the behavior of the virga range is the relationship between  $\bar{r}_d$  and  $r_a$  (Figure 3a). We assess this relationship by determining

$$\frac{d\ln(\bar{r}_d)}{d\ln(r_a)} = \frac{d\ln(\bar{M}_d)}{d\ln(M_a)} \equiv \delta, \quad (2)$$

where  $\delta$  describes the degree of correlation. Note that this correlation holds for  $\bar{r}_d$  and  $r_a$ , as well as the individual droplet and aerosol masses  $\bar{M}_d = (4/3)\pi\bar{r}_d^3\rho_d$  and  $M_a = (4/3)\pi r_a^3\rho_a$ , with  $\rho_d$  and  $\rho_a$  the densities of liquid water and the aerosol, respectively. In the initial range,  $\delta \approx 0$ , that is, there is no correlation between  $\bar{r}_d$  and  $r_a$ . This is expected because only a small fraction of aerosol particles activate to cloud droplets in this range, and the unactivated aerosol particles (haze) contribute only minute amounts of liquid water to  $\bar{r}_d$ . For the precipitation range,  $\delta$  approaches 1 (continuous gray line in Figure 3a), which indicates that every collision-coalescence event that increases  $\bar{M}_d$  leads to a commensurate increase in  $M_a$ . In the virga range, however,  $\delta \approx 0.5$  (dashed gray line in Figure 3a). This indicates that changes in  $\bar{r}_d$  are not completely determined by collision-coalescence. In fact,  $\Delta t_{\text{coll}} \approx 5000$  s in the virga range (Figure 3c), which is somewhat larger than the large-eddy boundary layer turnover time of about 3,000 s, calculated from the boundary layer depth and the boundary-layer-averaged vertical velocity standard deviation (e.g., Kogan, 2006). If one assumes that all hydrometeors follow this large-eddy circulation spanning the entire boundary layer, aerosol particles in the virga range participate in collision-coalescence events about every second circulation only. Thus, a sustained effect on  $\bar{r}_d$  by collision-coalescence is prevented because these particles fully evaporate when they leave the cloud, either by following the large-eddy circulation, sedimentation, or both. (This justifies our use of the term virga for this part of the aerosol size distribution.) Note that although collision-coalescence is infrequent (Figure 3c),  $r_a$  has a constant rate of increase in the virga range, as shown by  $\bar{c}_a$  (Figure 3b).

Within the virga range, collision-coalescence processing does not substantially depend on  $r_a$ , as shown by the limited variability in  $\bar{c}_a$  and  $\Delta t_{\text{coll}}$  with  $r_a$  (Figures 3b and 3c). But when the aerosol particles are larger, their ability to activate to cloud droplets is greater (blue line in Figure 3d), which increases the likelihood that these particles participate in more collision-coalescence events per large-eddy circulation cycle. Additionally, it is expected that the greater aerosol-loading with larger  $r_a$  causes stronger condensational growth (e.g., Jensen & Nugent, 2017). Both effects are reflected in the moderately increasing  $\bar{r}_d$  with  $r_a$  in the virga range. This behavior continues until  $\bar{r}_d$  exceeds 40  $\mu\text{m}$ , marking the beginning of the precipitation range, where collision-coalescence forms drops that do not evaporate fully below cloud base and eventually reach the surface, which manifests in the strong increase in the net collision gain and precipitation loss rates (orange and red lines in Figure 3d). The figures in Supporting Information S1 show that  $\bar{r}_d > 40$   $\mu\text{m}$  also limits the virga range for other initial aerosol size distributions, proving the efficacy of the  $\bar{r}_d \approx 40$   $\mu\text{m}$  threshold that is used in some bulk cloud microphysical models to delineate drops with progressively increasing collection efficiency (e.g., Kessler, 1969; Seifert & Beheng, 2006).

### 3. Theory

To better understand the virga and precipitation ranges shown in Figures 2 and 3, we develop a theory that explains some of the modeled processes. For this, we evaluate a prognostic equation for the aerosol mass distribution  $m_a = M_a n_a$ . We start with

$$\frac{dm_a}{dt} = \frac{\partial m_a}{\partial t} + c_a \frac{\partial m_a}{\partial r_a} = P, \quad (3)$$

where  $P$  covers sources and sinks, that is, the loss of aerosol mass through precipitation scavenging in this study (red line in Figure 3d). The change in aerosol mass through collision-coalescence is included in the advection term  $c_a \partial m_a / \partial r_a$ , as it does not create or remove aerosol mass, but moves aerosol mass in the  $r_a$  space only (orange line in Figure 3d).

For simplicity, we will assume stationarity ( $\partial m_a / \partial t = 0$ ) in the virga and the precipitation range. For this to be true, the net collision gain rate and the precipitation loss rates must be equal (cf. Figure 3d). While this is approximately the case in the precipitation range, the virga range violates this assumption. However, the actual changes in the virga range are relatively slow ( $\sim 1$  hr) because the net collision gain rate is small and the precipitation loss rate is essentially negligible. Potential limitations due to this simplification are discussed below. Assuming stationarity, we rewrite Equation 3 as

$$\frac{\partial \ln(m_a)}{\partial \ln(r_a)} = \frac{r_a}{m_a c_a} P. \quad (4)$$

We assume that  $P$  is proportional to the sedimentation velocity  $w_{\text{sed}}$  of the droplets carrying the aerosol, as well as inversely proportional to the average height  $z_c$  from which the droplets are falling. We estimate that  $z_c = (z_t - z_b)/2$ , where  $z_t$  and  $z_b$  are the cloud top and base heights, respectively. Thus, we write

$$P = -m_a \frac{w_{\text{sed}}(\bar{r}_d)}{z_c}. \quad (5)$$

Note that  $w_{\text{sed}}$  is an effective sedimentation velocity, taking into account the averaging necessary to obtain  $\bar{r}_d$ . Note further that we ignore the fact that droplets evaporate below cloud base.

To establish an expression for  $c_a$ , we need to express aerosol growth by droplet growth. For this, we determine the temporal derivative of Equation 2, yielding

$$c_a = \frac{dr_a}{dt} = \frac{1}{\delta} \frac{r_a}{\bar{r}_d} \frac{d\bar{r}_d}{dt}, \quad (6)$$

similar to Feingold et al. (1996). The continuous collision-coalescence growth model by Bowen (1950), see Equation 8.15 in Rogers and Yau (1989), which represents the growth of one droplet collecting others, is used to express  $d\bar{r}_d/dt$ . With Equation 6, it follows that

$$c_a = \frac{1}{\delta} \frac{r_a}{\bar{r}_d} \left[ \frac{E \text{LWC}}{4\rho_d} w_{\text{sed}}(\bar{r}_d) \right], \quad (7)$$

where  $E$  is an average collision efficiency, and LWC the liquid water content of the collected cloud droplets. Again,  $w_{\text{sed}}$  is an effective sedimentation velocity, accounting for the necessary averaging to obtain  $\bar{r}_d$ .

Using expressions Equations 5 and 7 in Equation 4, we get

$$\frac{\partial \ln(m_a)}{\partial \ln(r_a)} = -\bar{r}_d \frac{4\rho_d}{E \text{LWC} z_c} \delta, \quad (8)$$

which can be rewritten as

$$\frac{\partial \ln(m_a)}{\partial \bar{r}_d} = -\frac{4\rho_d}{E \text{LWC} z_c}, \quad (9)$$

using Equation 2. Note that this expression does not depend on  $w_{\text{sed}}$ .

Assuming that  $E$ , LWC, and  $z_c$  are constant for all  $r_a$ , integration yields

$$m_a(r_a) = m_a(r_{a,0}) \exp \left\{ -[\bar{r}_d(r_a) - \bar{r}_d(r_{a,0})] \frac{4\rho_d}{E \text{LWC} z_c} \right\}, \quad (10)$$

where  $r_{a,0}$  is the aerosol radius that defines the constants of integration. The corresponding analytical  $n_a^e$  are shown in Figure 2 (orange lines), for which appropriate values for  $m_a(r_{a,0})$ ,  $E$ , LWC, and  $z_c$  are estimated. For  $r_{a,m} = 25$  nm,  $\bar{r}_d$  is obtained from Figure 3a, while corresponding data is used for  $r_{a,m} = 12.5$  and 50 nm. As the analytical solution does not capture the initial distribution, only values in the virga and precipitation range are shown.

Overall, the analytic solution captures the decrease of  $n_a^e$  in the precipitation regime well. It also captures the constant slope in the virga range, the approximate values of which are indicated in Figure 2 (continuous gray lines). However, the slope of the analytical solution is too negative in comparison. This indicates that the analytic solution is too simplistic to account for the processes happening in the virga range, where the evaporation of droplets below cloud base plays an important role in decelerating aerosol growth before entering the precipitation range. Furthermore, the cessation of the supply of aerosol mass for collision-coalescence processing from the initial range violates the steady state assumption for the virga and precipitation ranges. Interestingly, for  $r_{a,m} = 12.5$  nm, the agreement between the analytical and numerical solution in the virga

range is much higher than for the other cases. This might be due to the larger reservoir of unactivated aerosol particles in the initial range that becomes available to collision-coalescence processing as time progresses. In fact, the slope of  $-1.8$  in the virga range of  $r_{a,m} = 12.5$  nm is much closer to  $-2$ , which would indicate a constant  $m_a$  and hence a constant aerosol mass flux ( $c_a m_a$ ) through the virga range toward the precipitation range.

#### 4. Summary

Aerosol-cloud-climate interactions are not only determined by the changes caused by the number and size of aerosol particles, but also by the effects of clouds on the aerosol size distribution. In this study, we analyzed the processing of aerosol by droplet collision-coalescence, which allows aerosol particles to merge into larger entities. To investigate this, we used a LCM coupled to a high-resolution LES model, representing a drizzling stratocumulus-topped boundary layer.

In agreement with previous studies, we find that the aerosol size distribution is shifted toward larger sizes due to collision-coalescence processing (e.g., Feingold et al., 1996; Flossmann et al., 1985; Hudson et al., 2018; Jaruga & Pawlowska, 2018; Lebo & Seinfeld, 2011; Schmeller & Geresdi, 2019). While these previous studies relied on an idealized zero- to two-dimensional representation of the cloud dynamics, our study is able to represent the full three-dimensional impact of the stratocumulus-topped boundary layer on the aerosol processing. We showed that these dynamics are essential for the development of a new processed aerosol mode (cf. Figure 2), which we termed the virga range of the aerosol size distribution as it requires the evaporation of cloud droplets below cloud base. Generally, aerosol particles follow the large-eddy circulation of the stratocumulus-topped boundary layer, and activate to cloud droplets inside the cloud layer, where they grow by condensation and might collide and coalesce with other droplets, leading to an increase in aerosol size. However, this increase is only moderate as long as cloud droplets leave the cloud and fully evaporate before further collision-coalescence events take place. As this cycle of condensation, potential collision-coalescence, and evaporation repeats, the growing aerosol accelerates droplet growth. Once a threshold of  $\sim 40$   $\mu\text{m}$  in cloud droplet radius is reached, multiple collisions inside the cloud are possible, triggering a substantial increase in droplet and aerosol size and the eventual loss of the affected particles to the surface as precipitation. Accordingly, we cannot define a maximum aerosol size bounding the virga range, but only an associated maximum droplet size.

The virga range is essential to the creation of a reservoir of larger aerosol particles in the atmosphere, and prevents their immediate loss to the surface via precipitation by the evaporation of cloud droplets below the cloud. Thus, the virga range weakens the clear relation between aerosol and cloud droplet mass caused by collision-coalescence processing that was highlighted in more idealized studies in the past (e.g., Feingold et al., 1996; Flossmann et al., 1985). Nonetheless, we find that a tight relation between aerosol and cloud droplet mass still holds for the strongly precipitating part of the aerosol size distribution, suggesting that more strongly precipitating clouds than those analyzed here might not exhibit a virga range. On the other hand, a low cloud fraction, typical of shallow cumulus clouds or open-cell stratocumulus, might extend the virga range by increasing the probability for droplet evaporation, and the formation of a stable population of giant aerosol particles, which have been frequently observed below trade-wind cumuli (e.g., Gerber et al., 2008).

We note that our study focuses on the processing of aerosol via cloud droplet collision-coalescence only, and is thus rather idealized in that regard. Future studies need to include the full aerosol processing through aqueous chemistry (e.g., Hegg & Hobbs, 1979), as well as the (rather weak) Brownian capture of unactivated aerosol particles by rain drops (e.g., Svenningsson et al., 1997). The LCM approach applied here might be the right tool for this inquiry.

#### Data Availability Statement

The System for Atmospheric Modeling (SAM) code is graciously provided by Marat Khairoutdinov, and available under the link <http://rossby.msfc.sunysb.edu/SAM.html>. Simulation results are available under the link <https://doi.org/10.5281/zenodo.7734008>.



Acknowledgments

FH appreciates support from the Emmy Noether program of the German Research Foundation (DFG) under Grant HO 6588/1-1. GF acknowledges funding from NOAA's ERB program (NOAA CPO Climate and CI 03-01-07-001). This research was supported in part by the National Science Foundation under Grant NSF PHY-1748958. Open Access funding enabled and organized by Projekt DEAL.

References

Ackerman, A. S., VanZanten, M. C., Stevens, B., Savic-Jovicic, V., Bretherton, C. S., Chlond, A., et al. (2009). Large-eddy simulations of a drizzling, stratocumulus-topped marine boundary layer. *Monthly Weather Review*, *137*(3), 1083–1110. <https://doi.org/10.1175/2008mwr2582.1>

Albrecht, B. A. (1989). Aerosols, cloud microphysics, and fractional cloudiness. *Science*, *245*(4923), 1227–1230. <https://doi.org/10.1126/science.245.4923.1227>

Arabas, S., Jaruga, A., Pawlowska, H., & Grabowski, W. (2015). libcloudph++ 1.0: A single-moment bulk, double-moment bulk, and particle-based warm-rain microphysics library in c++. *Geoscientific Model Development*, *8*(6), 1677–1707. <https://doi.org/10.5194/gmd-8-1677-2015>

Beard, K. V. (1976). Terminal velocity and shape of cloud and precipitation drops aloft. *Journal of the Atmospheric Sciences*, *33*(5), 851–864. [https://doi.org/10.1175/1520-0469\(1976\)033<0851:tvasoc>2.0.co;2](https://doi.org/10.1175/1520-0469(1976)033<0851:tvasoc>2.0.co;2)

Berner, A., Bretherton, C., Wood, R., & Muhlbauer, A. (2013). Marine boundary layer cloud regimes and POC formation in a CRM coupled to a bulk aerosol scheme. *Atmospheric Chemistry and Physics*, *13*(24), 12549–12572. <https://doi.org/10.5194/acp-13-12549-2013>

Bowen, E. (1950). The formation of rain by coalescence. *Australian Journal of Chemistry*, *3*(2), 193–213. <https://doi.org/10.1071/ch9500193>

Bretherton, C., Blossey, P. N., & Uchida, J. (2007). Cloud droplet sedimentation, entrainment efficiency, and subtropical stratocumulus albedo. *Geophysical Research Letters*, *34*(3), L03813. <https://doi.org/10.1029/2006gl027648>

Chandrakar, K. K., Morrison, H., & Witte, M. (2022). Evolution of droplet size distributions during the transition of an ultraclean stratocumulus cloud system to open cell structure: An LES investigation using Lagrangian microphysics. *Geophysical Research Letters*, *49*(17), e2022GL100511. <https://doi.org/10.1029/2022gl100511>

Feingold, G., Kreidenweis, S. M., Stevens, B., & Cotton, W. (1996). Numerical simulations of stratocumulus processing of cloud condensation nuclei through collision-coalescence. *Journal of Geophysical Research*, *101*(D16), 21391–21402. <https://doi.org/10.1029/96jd01552>

Flossmann, A. I., Hall, W., & Pruppacher, H. (1985). A theoretical study of the wet removal of atmospheric pollutants. Part I: The redistribution of aerosol particles captured through nucleation and impaction scavenging by growing cloud drops. *Journal of the Atmospheric Sciences*, *42*(6), 583–606. [https://doi.org/10.1175/1520-0469\(1985\)042<0583:atsotw>2.0.co;2](https://doi.org/10.1175/1520-0469(1985)042<0583:atsotw>2.0.co;2)

Gerber, H. E., Frick, G. M., Jensen, J. B., & Hudson, J. G. (2008). Entrainment, mixing, and microphysics in trade-wind cumulus. *Journal of the Meteorological Society of Japan*, *86*, 87–106. <https://doi.org/10.2151/jmsj.86a.87>

Hall, W. D. (1980). A detailed microphysical model within a two-dimensional dynamic framework: Model description and preliminary results. *Journal of the Atmospheric Sciences*, *37*(11), 2486–2507. [https://doi.org/10.1175/1520-0469\(1980\)037<2486:admmwa>2.0.co;2](https://doi.org/10.1175/1520-0469(1980)037<2486:admmwa>2.0.co;2)

Hegg, D. A., & Hobbs, P. V. (1979). The homogeneous oxidation of sulfur dioxide in cloud droplets. *Atmospheric Environment*, *13*(7), 981–987. [https://doi.org/10.1016/0004-6981\(79\)90008-8](https://doi.org/10.1016/0004-6981(79)90008-8)

Hill, A. A., Lebo, Z. J., Andrejczuk, M., Arabas, S., Dziekan, P., Field, P., et al. (2023). Toward a numerical benchmark for warm rain processes. *Journal of the Atmospheric Sciences*, *80*(5), 1329–1359. <https://doi.org/10.1175/jas-d-21-0275.1>

Hoffmann, F., Noh, Y., & Raasch, S. (2017). The route to raindrop formation in a shallow cumulus cloud simulated by a Lagrangian cloud model. *Journal of the Atmospheric Sciences*, *74*(7), 2125–2142. <https://doi.org/10.1175/jas-d-16-0220.1>

Hoffmann, F., Raasch, S., & Noh, Y. (2015). Entrainment of aerosols and their activation in a shallow cumulus cloud studied with a coupled LCM-LES approach. *Atmospheric Research*, *156*, 43–57. <https://doi.org/10.1016/j.atmosres.2014.12.008>

Hoppel, W., Frick, G., & Larson, R. (1986). Effect of nonprecipitating clouds on the aerosol size distribution in the marine boundary layer. *Geophysical Research Letters*, *13*(2), 125–128. <https://doi.org/10.1029/gl013i002p00125>

Hudson, J. G., & Noble, S. (2020). CCN spectral shape and cumulus cloud and drizzle microphysics. *Journal of Geophysical Research: Atmospheres*, *125*(1), e2019JD031141. <https://doi.org/10.1029/2019jd031141>

Hudson, J. G., & Noble, S. (2022). CCN spectral modality compared to droplet spectra and drizzle in RICO cumuli. *Journal of Geophysical Research: Atmospheres*, *127*(24), e2022JD037189. <https://doi.org/10.1029/2022jd037189>

Hudson, J. G., Noble, S., & Tabor, S. (2018). CCN spectral shape and stratus cloud and drizzle microphysics. *Journal of Geophysical Research: Atmospheres*, *123*(17), 9635–9651. <https://doi.org/10.1029/2017jd027865>

Jaenicke, R. (1993). Tropospheric aerosols. *International Geophysics*, *54*, 1–31.

Jaruga, A., & Pawlowska, H. (2018). libcloudph++ 2.0: Aqueous-phase chemistry extension of the particle-based cloud microphysics scheme. *Geoscientific Model Development*, *11*(9), 3623–3645. <https://doi.org/10.5194/gmd-11-3623-2018>

Jensen, J. B., & Nugent, A. D. (2017). Condensational growth of drops formed on giant sea-salt aerosol particles. *Journal of the Atmospheric Sciences*, *74*(3), 679–697. <https://doi.org/10.1175/jas-d-15-0370.1>

Kessler, E. (1969). On distribution and continuity of water substance in atmospheric circulations. *Meteorological Monographs*, *10*, 84.

Khairoutdinov, M. F., & Randall, D. A. (2003). Cloud resolving modeling of the ARM summer 1997 IOP: Model formulation, results, uncertainties, and sensitivities. *Journal of the Atmospheric Sciences*, *60*(4), 607–625. [https://doi.org/10.1175/1520-0469\(2003\)060<0607:crmota>2.0.co;2](https://doi.org/10.1175/1520-0469(2003)060<0607:crmota>2.0.co;2)

Kogan, Y. L. (2006). Large-eddy simulation of air parcels in stratocumulus clouds: Time scales and spatial variability. *Journal of the Atmospheric Sciences*, *63*(3), 952–967. <https://doi.org/10.1175/jas3665.1>

Köhler, H. (1936). The nucleus in and the growth of hygroscopic droplets. *Transactions of the Faraday Society*, *32*(0), 1152–1161. <https://doi.org/10.1039/tf9363201152>

Lebo, Z., & Seinfeld, J. (2011). A continuous spectral aerosol-droplet microphysics model. *Atmospheric Chemistry and Physics*, *11*(23), 12297–12316. <https://doi.org/10.5194/acp-11-12297-2011>

Noble, S. R., & Hudson, J. G. (2019). Effects of continental clouds on surface Aitken and accumulation modes. *Journal of Geophysical Research: Atmospheres*, *124*(10), 5479–5502. <https://doi.org/10.1029/2019jd030297>

Rogers, R. R., & Yau, M. K. (1989). *A short course in cloud physics*. Pergamon Press.

Schmeller, G., & Geresdi, I. (2019). Study of interaction between cloud microphysics and chemistry using coupled bin microphysics and bin aqueous chemistry scheme. *Atmospheric Environment*, *198*, 366–380. <https://doi.org/10.1016/j.atmosenv.2018.10.064>

Seifert, A., & Beheng, K. D. (2006). A two-moment cloud microphysics parameterization for mixed-phase clouds. Part I: Model description. *Meteorology and Atmospheric Physics*, *92*(1–2), 45–66. <https://doi.org/10.1007/s00703-005-0112-4>

Shima, S.-I., Kusano, K., Kawano, A., Sugiyama, T., & Kawahara, S. (2009). The super-droplet method for the numerical simulation of clouds and precipitation: A particle-based and probabilistic microphysics model coupled with a non-hydrostatic model. *Quarterly Journal of the Royal Meteorological Society*, *135*(642), 1307–1320. <https://doi.org/10.1002/qj.441>

Squires, P. (1958). The microstructure and colloidal stability of warm clouds: Part I—The relation between structure and stability. *Tellus*, *10*(2), 256–261. <https://doi.org/10.1111/j.2153-3490.1958.tb02011.x>

Stevens, B., Lenschow, D. H., Vali, G., Gerber, H., Bandy, A., Blomquist, B., et al. (2003). Dynamics and chemistry of marine stratocumulus—DYCOMS-II. *Bulletin American Meteorological Society*, *84*(5), 579–594.

- Svenningsson, B., Hansson, H.-C., Martinsson, B., Wiedensohler, A., Swietlicki, E., Cederfelt, S.-I., et al. (1997). Cloud droplet nucleation scavenging in relation to the size and hygroscopic behaviour of aerosol particles. *Atmospheric Environment*, *31*(16), 2463–2475. [https://doi.org/10.1016/s1352-2310\(96\)00179-3](https://doi.org/10.1016/s1352-2310(96)00179-3)
- Twomey, S. (1977). The influence of pollution on the shortwave albedo of clouds. *Journal of the Atmospheric Sciences*, *34*(7), 1149–1152. [https://doi.org/10.1175/1520-0469\(1977\)034<1149:tiopot>2.0.co;2](https://doi.org/10.1175/1520-0469(1977)034<1149:tiopot>2.0.co;2)
- Unterstrasser, S., Hoffmann, F., & Lerch, M. (2020). Collisional growth in a particle-based cloud microphysical model: Insights from column model simulations using lcm1d (v1. 0). *Geoscientific Model Development*, *13*(11), 5119–5145. <https://doi.org/10.5194/gmd-13-5119-2020>
- Wang, S., Wang, Q., & Feingold, G. (2003). Turbulence, condensation, and liquid water transport in numerically simulated nonprecipitating stratocumulus clouds. *Journal of the Atmospheric Sciences*, *60*(2), 262–278. [https://doi.org/10.1175/1520-0469\(2003\)060<0262:tcawt>2.0.co;2](https://doi.org/10.1175/1520-0469(2003)060<0262:tcawt>2.0.co;2)
- Weil, J. C., Sullivan, P. P., & Moeng, C.-H. (2004). The use of large-eddy simulations in Lagrangian particle dispersion models. *Journal of the Atmospheric Sciences*, *61*(23), 2877–2887. <https://doi.org/10.1175/jas-3302.1>
- Zeng, X., & Li, X. (2023). Explicitly modeling the effects of cloud condensation nuclei on warm rain initiation. *Journal of the Atmospheric Sciences*, *80*(1), 259–272.